Improved Laser-Induced Defect Passivation and Simultaneous Elimination of Light-Induced Degradation in p-Type Czochralski Silicon

Arman Mahboubi Soufiani, Anastasia Soeriyadi, Catherine Chan, and Brett Hallam, *Member, IEEE*

***Abstract*—Laser doping is a typical industrial method to introduce a local highly doped region in silicon solar cells to form a selective emitter. Such a process inherently introduces defects that can be a concern to the overall performance of the solar cell. Here, we investigate the effectiveness of laser-induced defect (LasID) passivation on lifetime test structures through different annealing processes, including high-temperature belt-furnace firing, low-temperature belt-furnace annealing, and an advanced hydrogenation process (AHP) for n^+ laser-doped selective emitters. We demonstrate clear advantages of post treatment using a rapid 10 s AHP at 300 °C when the lifetime structures are prefired. For the examined laser speeds of 0.5–6 m/s (sheet resistances of 4–70 Ω/□), AHP is the most effective treatment method. For example, for a typical laser doping speed of 4 m/s, starting from the same effective carrier lifetime of 36.9±2.4 μs after laser-doping step for all the passivation treatments, the AHP not only surpasses the conventional approaches by showing the highest recovery of the effective carrier lifetime (∼79% compared with ∼63% and ∼41% for the firing and belt-furnace annealing treatments, respectively) and dark saturation current density reduction in the regions affected by LasIDs but also simultaneously suppresses light-induced degradation (maximum of 4% effective lifetime degradation with respect to the passivated state, as opposed to 14% and 16% degradation for the firing and belt-furnace annealing treatments, respectively) common in Cz grown boron-doped p-type monocrystalline silicon.**

***Index Terms*—Hydrogen passivation, laser doping, laser-induced defect (LasID), light-induced degradation (LID), selective emitter.**

I. Introduction

SELECTIVE emitter structures have been used as effective pathways to enhance the performance of both n-type and p-type silicon solar cells [1]–[6].

While high-temperature diffusion and photolithography-based techniques have been used to fabricate high-efficiency selective emitter silicon cells of different architectures [7], [8], the low throughput and energy- and cost-intensive steps involved prevent their industrial implementation for mass production. An industrially feasible alternative approach is laser doping. According to the International Technology Roadmap for Photovoltaic (ITRPV 2020), laser-doped selective emitters (LDSE) are predicted to constitute more than 80% market share of phosphorous emitter technologies for p-type solar cells by 2030 [9].

Laser doping is commonly implemented in two ways. In the current industrial approach for passivated emitter and rear cells (PERC), the unpassivated, diffused silicon wafer is laser doped directly after phosphorus diffusion using the phosphosilicate glass (PSG) layer as the dopant source. After PSG removal and emitter rear etch, surface passivating/antireflection coating dielectric(s) are deposited [10]. Subsequently, an aligned screen-printing process is performed. During firing, the metal contact paste penetrates through the dielectrics to contact the underlying laser-doped silicon region. This process has been used by LONGi to achieve average production efficiencies over 22.5% and peak efficiency of 23.83% [11]. To enable sufficient yields with the current alignment capability of screen printers, the laser-doped region is wider (∼100 μm) than the aligned metal finger (∼40 μm). Alternatively, the laser-doping process can be performed after dielectric deposition whereby the laser-doping process simultaneously creates local contact openings through the dielectric stack and incorporates dopants into the local area of the underlying silicon. Using this approach, metallization is typically performed through a self-aligned plating method [12]. This approach was used by Suntech to achieve the first commercial p-type Cz solar cell efficiency of over 20% in 2012 [13]. However, it is also possible to subsequently align screen-printed contacts using a nonfire-through paste. One potential advantage of performing laser doping after dielectric deposition is a significant reduction in total laser-doping area coverage and metal/silicon interface area [14], thereby reducing the device's recombination parameter (J_0), leading to noticeable open-circuit voltage (V_{OC}) gains.

A major downside of employing laser doping, in general, is that it creates recombination active defects [15] within the heavily doped molten region, at the boundary of the solid/molten region and at silicon/dielectric interfaces, even when laser processing conditions are optimized. The laser-induced defects (LasIDs) degrade the bulk and surface charge–carrier lifetimes,

Manuscript received June 8, 2021; revised August 3, 2021; accepted August 10, 2021. Date of publication September 7, 2021; date of current version October 21, 2021. This work was supported in part by Australian Government through the Australian Renewable Energy Agency under Project 2017/RND010 and Project 2020/RND005 and in part by the Australian Centre for Advanced Photovoltaics (ACAP) under Grant 1-SRI001. The work of Arman Mahboubi Soufiani was partly supported by ACAP under Grant RG193402-I. *(Corresponding author: Brett Hallam.)*

The authors are with the School of Photovoltaic and Renewable Energy Engineering, University of New South Wales, Sydney, NSW 2052, Australia (e-mail: armansoufiani@gmail.com; anastasia.soeriyadi@unsw.edu.au; catherine.chan@unsw.edu.au; brett.hallam@unsw.edu.au).

Color versions of one or more figures in this article are available at https://doi.org/10.1109/JPHOTOV.2021.3104765.

Digital Object Identifier 10.1109/JPHOTOV.2021.3104765

which reduce the solar cell performance [16]. Earlier studies proposed that the melting and recrystallization processes during lasing introduce impurities, such as oxygen, carbon, and nitrogen, into the laser-doped region, forming new recombination centers [17]. A recent study suggested that a large number of emissive dislocations in the edge area of the laser-doped region and to a lesser extent in the fully molten highly doped central region may form during the solidification phase of the molten silicon [18]. Ernst *et al*. [19] associated the large decrease in the carrier lifetime of the laser-doped region mainly with the edge areas around the central fully molten region. The contribution of the fully molten heavily doped region was calculated to be less but not negligible. Estimated J_0 values reported for the edge areas were at least three times larger than that of the fully molten region. Thermal expansion mismatch between silicon and overlying dielectrics, such as silicon nitride, has also been proposed as a cause of LasID formation [20].

One possible remedy to minimize this laser-doped region edge recombination is the above-mentioned process of laser doping prior to the dielectric deposition that allows coverage of the edges with passivating dielectric layers [21], [22]. When laser doping is performed through the dielectric stack, the induced damage, including the edge damage, is expected to intensify. Applying effective defect passivation methods is necessary for both laser-doping approaches.

A common approach to mitigate the impact of LasIDs through passivation is to apply a post thermal treatment. Industrial LDSE PERC solar cells with laser doping performed before dielectric deposition have the benefit that a firing process is performed after dielectric deposition, thereby creating scope for hydrogen passivation of LasIDs. On the other hand, if laser doping is performed after the firing of dielectric layers, a potential opportunity for the passivation of LasIDs is missed. However, it has been shown that short (<5 min) low-temperature (400–500 °C) belt-furnace annealing (BFA) can improve the performance of typical LDSE solar cells with full-area aluminum back surface field structure by ∼0.36% absolute, where laser doping and BFA are performed after the firing step [23]. A performance improvement for front laser-doped n-PERT solar cells of up to 0.84% has also been reported through applying BFA [23], partly due to a considerable reduction in the J_0 associated with the laser-doped region. Another approach for passivating the defects created by laser doping is the implementation of a laser-annealing process. A second pass of lasing is run over the laser-doped region at much lower laser power to anneal the damage induced in the first high-power laser-doping pass [24], [25].

Another key challenge for p-type Cz LDSE PERC solar cells is light-induced degradation (LID) associated with boron–oxygen (B–O) defects [26]–[29]. Fortunately, B–O defects also respond to thermal annealing. In particular, illuminated annealing, first reported by Herguth *et al*. [30], can electrically neutralize the defects, almost fully eliminate B–O LID [28], [30] owing to the improved mobility and reactivity of hydrogen [34]. This process requires the presence of hydrogen in the bulk silicon to enable defect passivation [31], which naturally occurs in silicon solar cells during the metallization firing process, which simultaneously releases hydrogen into the bulk from the hydrogenated dielectrics. As such, after firing, an advanced hydrogenation process (AHP) incorporating illumination or minority carrier injection can be performed to passivate the B–O defects [30], [32], [33]. Recent work has demonstrated the complete elimination of B–O LID with an 8 s AHP [35]. High-temperature firing has also been reported to reduce the extent of B–O LID [28], [36], [37], although not completely eliminate it.

In this study, we compare the effectiveness of different annealing processes for the passivation of LasIDs created upon laser doping after the dielectric deposition and firing steps. In particular, we assess the impact of a low-temperature BFA (hereafter, 400 °C annealing), a fast-firing process with a peak temperature of 680 °C (hereafter, 680 °C firing), as well as a rapid high intensity 10 s illuminated annealing process (i.e., AHP) at 300 °C on passivating the LasIDs for n^+ laser-doped regions on monocrystalline p-type Cz wafers. We then investigate the impact of these passivation processes for their effectiveness in simultaneously reducing susceptibility to LID.

II. Experimental Details

Textured p-type Cz wafers with thicknesses and base resistivities of approximately 167 μm and 1.55 Ω·cm, respectively, were used in this experiment. All samples were gettered in a $POCl_3$ tube TEMPRESS furnace by heavy diffusion at 840 °C for 45 min with a resulting sheet resistance of approximately 40 Ω/sq. Then, KOH retexturing was performed to remove 4 μm silicon from each side of the wafers to remove the gettering diffusion. A lightly diffused emitter profile was then created in a $POCl_3$ tube furnace at 770 °C for 25 min followed by a drive-in diffusion at 810 °C for 25 min in nitrogen ambient and then at 880 °C for 40 min in oxygen ambient. The sheet resistance after this diffusion process was 134±7 Ω/sq. Plasma-enhanced chemical vapor deposition (PECVD) (MAiA from Roth and Rau) was then used to deposit a 75 nm thick hydrogenated silicon nitride (SiN_x:H) layer—with a refractive index of 2.08 at 633 nm—on both sides of the symmetrical lifetime structures [38].

All lifetime samples used in this study went through an initial firing step with a peak measured temperature of 680 °C in an industrial CAMiNI furnace from Roth and Rau, with the temperature profile shown in Fig. 1. The firing process was used to release hydrogen atoms from the PECVD SiN_x:H layer and distribute hydrogen throughout the silicon bulk [39]–[41], which is required for subsequent low-temperature hydrogen passivation processes, as well as passivation of some background defects to allow for a clearer understanding of the specific impact of various passivation techniques on the defects formed by laser doping.

To create the heavily doped n^+ profiles, 85% H_3PO_4 (from J. T. Baker) was spun onto the wafer as a dopant source (6000 r/min for 40 s) prior to laser doping with a continuous-wave 532 nm Spectra Physics Millennia Prime laser. The laser power was measured at ∼14 W at the sample surface with an illumination spot size of about 20 μm (D4σ). Patterned boxes of 50 × 50 mm were formed filled with laser lines spaced 500 μm apart, with different laser scan speeds (0.5, 1, 2, 3, 4, and 6 m/s).

The laser patterns were created on three quadrants of a wafer for each laser speed; one quadrant did not receive laser doping,

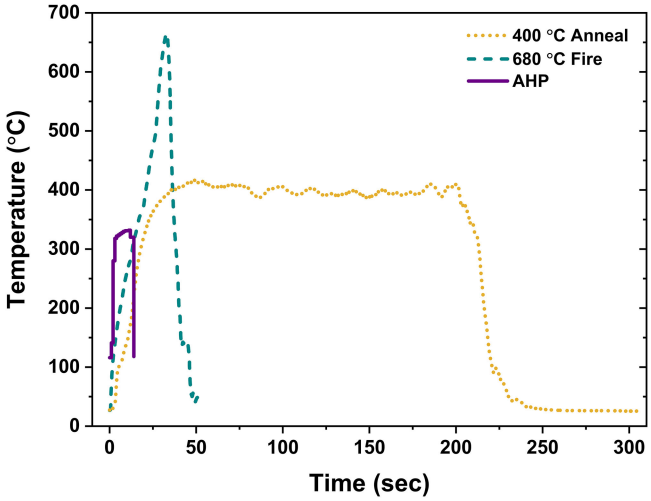

Fig. 1. Temperature profiles used in this work: 400 °C furnace annealing (dotted line), 680 °C furnace firing (dashed line), and AHP (solid line).

and this quadrant acted as the control sample throughout the processing sequences. Hereafter, the regions of the wafers with laser-doping pattern are denoted as the laser-doped samples, while the regions immediately affected by laser doping, the laser-doped lines, are referred to as laser-doped regions. Unless otherwise stated, the three laser-doped samples with the same laser-doping condition are used to calculate the uncertainty in the associated results. Optical microscope images were used to determine the extent of laser damage caused by laser doping (i.e., laser-doped line widths including the not fully melted edge area) and thus to calculate the area fraction of laser-doped regions.

To analyze the doping profile of the laser-doped regions, a series of 1 × 1 cm boxes were made by overlapping laser-doped lines. The sheet resistances and the doping profiles were measured using Sherescan four-point probe and WEP CVP21 electrochemical capacitance voltage (ECV) method, respectively, and are presented in Fig. 2. The measured doping profiles were then used as input to semiconductor software EDNA 2 (available on PV Lighthouse) to model the emitter total recombination current density [42], [43] associated with the laser-doped regions for various silicon surface recombination velocities (SRVs). For the simulation purposes, since the measured dopant density profiles started at a nonzero depth position with respect to the surface, a similar dopant density as that associated with this first position value was used for the zero-position dopant density.

The three post-treatment passivation approaches were investigated. A ∼3 min 400 °C annealing process and a 680 °C fast-firing process (the same as the first firing process) were performed in the CAMiNI firing furnace. A 10 s AHP was performed in a DR Laser AHP tool, where the silicon wafer was placed on a vacuum stage set at 300 °C and subjected to 960 nm laser illumination with an irradiance of about 56 kW/m^2 [32]. The corresponding temperature profiles are presented in Fig. 1.

To test for LID, an accelerated degradation test [33], [44] was performed using the same commercial laser system (DR Laser) as for AHP with the exception that the temperature of the

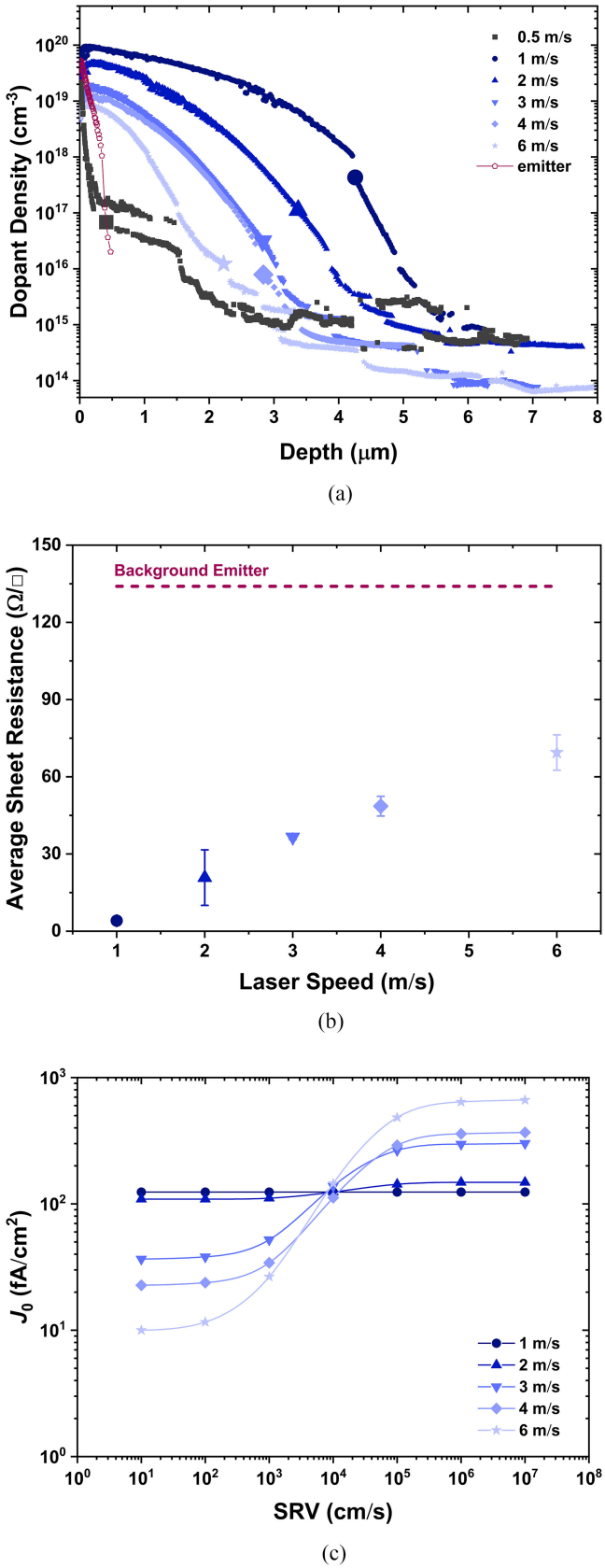

Fig. 2. (a) Dopant density profiles associated with a range of laser speeds used in this study with a fixed laser power of ∼14 W. (b) Average sheet resistance with respect to the laser speeds. (c) Simulated J_0 for emitters adapting the experimental n-type dopant profiles presented in panel (a) as a function of the SRV.

sample stage was held at 150 °C during the 10 s laser illumination. Similar processing conditions have been demonstrated to both accelerate LID in p-type monocrystalline silicon [33] and light- and elevated temperature-induced degradation (LeTID) in p-type multicrystalline silicon [44].

Injection-level dependent lifetime analysis was performed at various stages of the experiment using the quasi-steady-state photoconductance technique (Sinton Instruments WCT-120) [45]. The effective lifetimes were corrected for intrinsic recombination using the article presented in [46]. Unless otherwise stated, lifetimes are reported at excess carrier density $\Delta n = 9.4 \times 10^{14}$ cm^{-3} (considering the bulk resistivities of the samples used in this study, this is 0.1 $\times$ the bulk dopant density, 9.4×10^{15} cm^{-3}). Where estimation of the lifetime-equivalent defect density (ΔN_{leq}) [47] is needed, it is calculated through the inverse of the bulk lifetime

$$\frac{1}{\tau_{\mathrm{bulk}}} = \frac{1}{\tau_{\mathrm{eff}}} - \frac{1}{\tau_{\mathrm{surface}}} \tag{1}$$

where τ_{eff} and τ_{surface} are the effective and surface minority carrier lifetimes, respectively. τ_{surface} is estimated through

$$\frac{1}{\tau_{\mathrm{surface}}} = J_{0e}\,\frac{[N_A + \Delta n]}{q n_i^2 W} \tag{2}$$

where J_{0e} is the total emitter recombination current density, and N_A, q, n_i, and W are the known bulk dopant density, elementary charge, intrinsic carrier density, and sample thickness, respectively. ΔN_{leq} is calculated in two instances: Once after the passivation step with respect to the as-fired state by subtracting the inverse of the bulk lifetime extracted after the as-fired state ($\frac{1}{\tau_{\mathrm{bulk,as-fired}}}$) from that of the after passivation state ($\frac{1}{\tau_{\mathrm{bulk,\ pass.}}}$) and once after the degradation step with respect to the passivation state by subtracting the inverse of the bulk lifetimes extracted after the passivation state from that of the after degradation state (i.e., $\frac{1}{\tau_{\mathrm{bulk,LID}}} - \frac{1}{\tau_{\mathrm{bulk,pass.}}}$), to assess the effectiveness of the passivation techniques in annihilating LasIDs and reducing LID, respectively. The bulk lifetimes used for the ΔN_{leq} calculation are extracted at a minority carrier density of 9.4×10^{14} cm^{-3}.

Where relevant, in the figures, the uncertainty associated with the data for the control samples, for the as-fired and laser-doped states, is calculated for 18 samples (six control samples associated with six laser speeds for three different passivation methods). The uncertainty of the control data points for the passivation and LID states is calculated for the six control samples of the six wafers having different laser speeds. The error bars related to the laser-doped samples at each laser speed for the as-fired and laser-doped states are calculated for nine samples (three laser-doped samples associated with each laser speed for three different passivation methods). For each laser speed of each passivation method, the error bars are calculated for three laser-doped samples.

III. Results and Discussion

A. Laser-Doping Profile Characteristics

Fig. 2(a) illustrates the profiles of the electrically active dopants created by different laser speeds. A junction depth of up to 5 μm was observed for 1 m/s. Increasing the laser head speed from 1 to 6 m/s resulted in a decrease in the surface dopant concentration as well as a shallower profile. Consistent with the ECV profiles, the sheet resistance measurement results, provided in Fig. 2(b), show an increase in the sheet resistance with laser speed. Sheet resistances as low as 4.1$\pm$0.9 $\Omega/\square$ and as high as 69.4$\pm$6.9 $\Omega/\square$ were achieved for laser scan speeds 1 m/s and 6 m/s, respectively, substantially lower than that of the surrounding emitter (134$\pm$7 $\Omega/\square$). The sheet resistances/dopant profiles obtained here are within the same range as our previous work using the same laser system, bearing in mind the differences in the dopant source, spin-coating conditions, and laser powers [5]. For the laser speed of 0.5 m/s, we could not measure a reasonable sheet resistance within the boxes. The dopant profile also does not follow the trend observed in Fig. 2(a). We note that for the 0.5 m/s from the ECV results [see Fig. 2(a)], a comparison between the doping profile of the background emitter and the laser-doped region at this lowest speed shows that the laser process seems to grind the surface without necessarily doping it. These results for 0.5 m/s are inconsistent with our previous observation using the same laser system [5]. Furthermore, as will be seen in Section III-B, the lowest effective lifetime degradation was obtained for the 0.5 m/s condition, indicating its effective doping profile. Hence, the box pattern created for the sheet resistance and the ECV measurement of this laser-doping condition may be inadvertently different from when performing single line laser doping used for effective lifetime measurements. Results from the rest of the laser speed parameters show the relevance of the laser-doping region to be further studied. Nevertheless, for the sake of completeness, we keep the results of the 0.5 m/s condition for further analysis.

The dopant profiles, as shown in Fig. 2(a), are then used to model the total recombination current density for a wide range of SRVs in Fig. 2(c). At lower laser speeds with higher surface dopant concentrations and deeper profiles, effective shielding of the minority carriers from recombination at the surface is realized at high SRVs ($>10^4$ cm/s) while becoming limited by Auger recombination. Their efficacy in surface passivation drops at lower SRVs ($<10^4$ cm/s) as compared with faster laser speed parameters, resulting in a J_0 that is primarily independent of the SRV. On the contrary, while field-effect passivation of the faster laser speed parameters is inefficient at high SRVs resulting in a larger total recombination current, the absence of Auger recombination dominance, in this case, leads to low recombination current at lower SRV cases. As such, slower speeds are expected to yield lower J_0 values for metallized regions with high SRVs.

B. Defect Passivation

The initial effective lifetime of the samples was within the range of 112$\pm$8 μs [see Fig. 3(a)]. After performing laser doping, the effective lifetimes, reported at the same minority carrier density, degraded. The degradation ranges from $\sim$20% for 0.5 m/s to 60%–70% for the higher laser speeds, $\geq$ 2 m/s, in line with previous results [5].

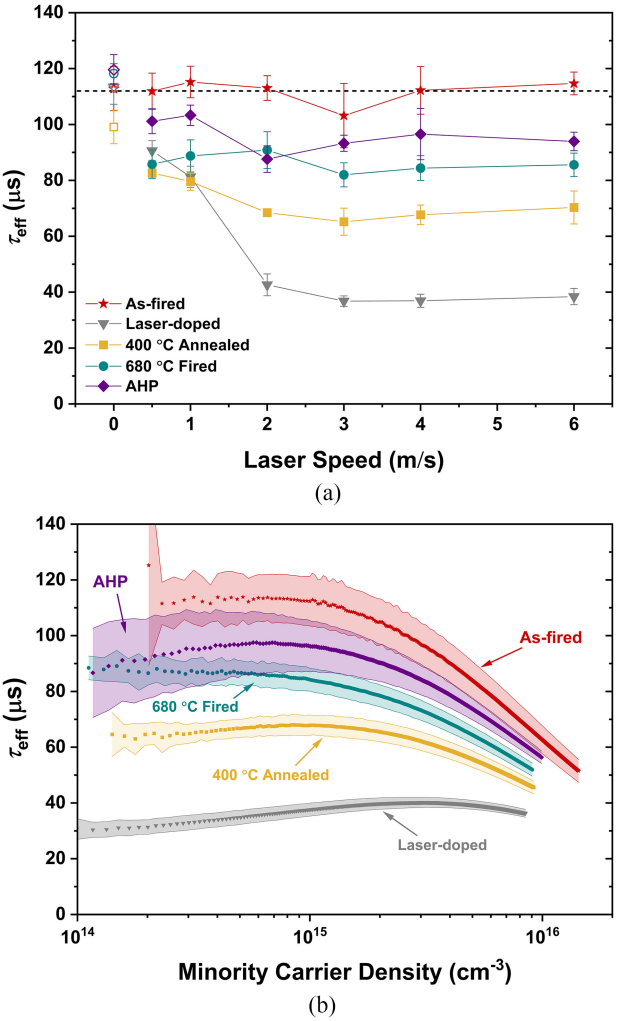

Fig. 3. Impact of different post-treatment methods on LasIDs passivation for n^+ laser-doped lifetime structures. (a) Presents the average effective lifetime values (extracted at 9.4×10^{14} cm^{-3}) at different stages of processing for different laser-doping conditions. The hollow symbols represent the control samples. The dashed line in panel (a) is a guide to eye marking the initial as-fired average effective lifetime, 112 μs. (b) Illustrates the example of effective lifetime curves versus minority carrier density for laser-doped samples with laser head scan speed of 4 m/s. The red symbol curve is the average effective lifetime curve of the as-fired state, and the shaded area is the uncertainty calculated for nine curves (three laser-doped samples for three passivation methods). The gray symbol curve and the associated shaded region are the average lifetime curve and the uncertainty calculated for the nine laser-doped samples (three laser-doped samples for three passivation methods). The average lifetime curve and the associated uncertainty of each LasID passivation approach are calculated for three laser-doped samples.

Upon passivation treatment, all approaches resulted in a noticeable lifetime increase. As shown in Fig. 3(a), the previously used approach of about 400 °C BFA [23] resulted in the smallest recovery of minority carrier lifetime after laser doping. The AHP resulted in the largest improvement in the effective lifetimes after laser doping for most of the laser conditions. Interestingly, AHP also led to a significant improvement in the effective lifetime of the laser-doped wafers with 0.5 m/s laser speed, whereas other passivation techniques did not. Average lifetime curves of the laser-doped samples, laser doped with a laser speed of 4 m/s, at each stage of processing are displayed in Fig. 3(b). This provides

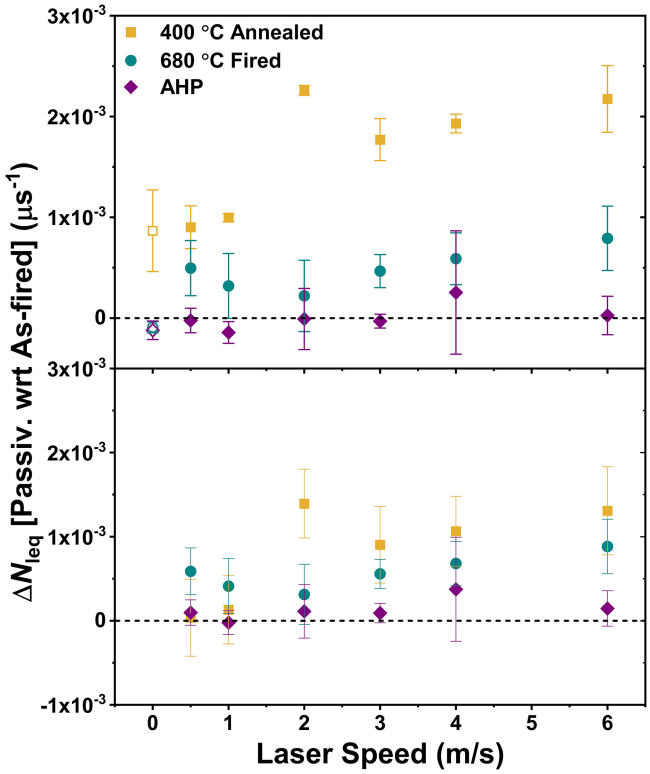

Fig. 4. (a) ΔN_{leq} values for the control and laser-doped samples calculated for the passivated state with respect to the initial fired state. (b) ΔN_{leq} values of the laser-doped samples are corrected for the contribution from the control samples ΔN_{leq} change (i.e., hollow data points in panel (a)).

a clear illustration of the effectiveness of the AHP treatment in passivating the laser damage. Starting from τ_{eff} of 36.9±2.4 μs after laser doping at 4 m/s, which is the same for all passivation approaches, only a 16.0±4.2 μs drop between the as-fired case to after laser doping and subsequent AHP (recovery of ∼79% from the laser-doped state) is obtained, compared with 27.8±3.6 μs (recovery of ∼63% from the laser-doped state) and 44.7±3.5 μs (recovery of ∼41% from the laser-doped state) for the 680 °C firing and 400 °C annealing, respectively.

These observations are better understood by evaluating the parameter, ΔN_{leq} [36]. The results are presented in Fig. 4(a). In general, ΔN_{leq}s should provide us with a better idea about the number of LasIDs remaining unpassivated in the bulk, formed, for instance, in the heat-affected zones [6]. It also incorporates any change in the background defects upon laser doping and subsequent passivation. The AHP treatment resulted in the lowest ΔN_{leq} compared with the 680 °C firing and 400 °C annealing approaches, indicating its effectiveness in passivating defects. However, it should be noted that the ΔN_{leq} of the laser-doped samples [filled symbols in Fig. 4(a)] also include changes in the effective defect density due to the formation and/or passivation of defects other than LasIDs (i.e., background defects). This is realized from the ΔN_{leq} of the control samples, as shown with hollow symbols in Fig. 4(a). Note that the change in the effective lifetime of the control samples after laser doping (i.e., after spin-coating spin-on dopant in the case of control samples) with respect to the as-fired state is minimal, therefore the ΔN_{leq} values

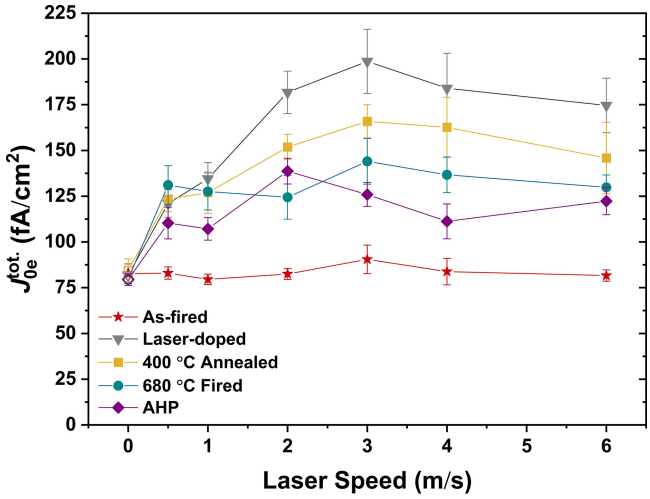

(a)

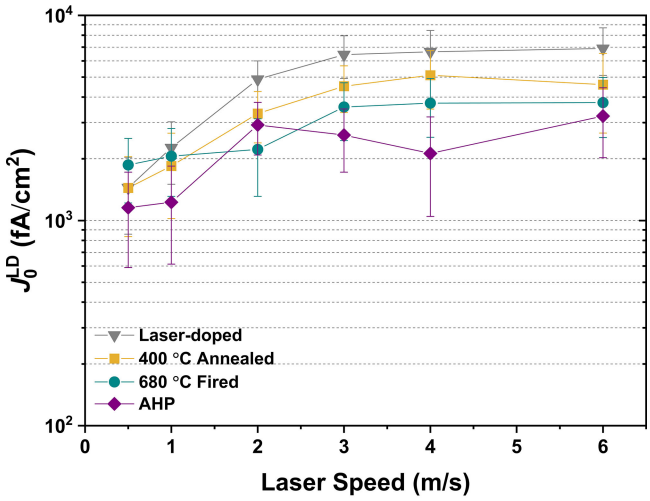

(b)

Fig. 5. (a) Total J_{0e} (combined J_0 of the laser-doped regions and the regions in between the laser lines) of the laser-doped side of the lifetime structures. The hollow data points represent the average of single-side J_{0e} of the control samples. For each stage of the processing except for the as-fired state, for which half the two-side J_{0e} at each speed is calculated, the single LD-side J_{0e} ($J_{0e}{}^{\text{tot.}}$) is calculated by subtracting the single-side J_{0e} of the control samples from the two-side J_{0e} of each laser speed (error propagation has been performed to calculate the error bars). (b) Estimate for the local J_0 of the laser-doped regions for after the laser-doping state and different passivation treatments. The error bars are calculated by propagating the error associated with each term in (3) of the main text, which considers a 10% error in the estimation of the laser line widths.

of the control samples can be assumed to be merely influenced by the passivation treatment processes. While some bulk defects are passivated by implementing AHP and the 680 °C firing methods, annealing at 400 °C activated some recombination active sites in the bulk increasing the corresponding ΔN_{leq} [see zero speed data points in Fig. 4(a)], while the total emitter recombination current density J_{0e} remains virtually unchanged in the control samples for all the treatment methods. The results related to J_{0e} are provided in Fig. 5 and will be discussed in the following text. To isolate the effects associated with the laser-doped lines themselves from those of regions not influenced by laser doping, assuming there is no interaction between the LasIDs and the other bulk defects modulated by the post-treatment passivation methods, ΔN_{leq} values, as presented in Fig. 4(a), are corrected for the control region's ΔN_{leq} changes. The results are depicted in Fig. 4(b). This plot further shows the advantage of AHP over the other two LasID passivation techniques, particularly the 400 °C annealing, in recovering the damage created by laser doping for almost all the laser speeds investigated. AHP results in ΔN_{leq} values, for instance, at the 4 m/s laser speed condition, lower than the 400 °C annealing and 680 °C firing on average by ∼57.1% and ∼19.7%, respectively. While Fig. 4(b) specifically elucidates the impact of each passivation technique on the laser-doping affected regions, the overall performance of a passivation technique on the whole range of defects in the silicon wafer, which is of industrial importance, also points to the pronounced benefit of implementing AHP after laser doping. We hypothesize that the manipulation of the hydrogen charge state in the AHP approach helps to passivate LasIDs as it does for other defects [34].

C. *Change in the Emitter Recombination Current Parameter*

Fig. 5(a) presents the total J_{0e} values $J_{0e}{}^{\text{tot.}}$ of the front laser-doped surfaces of the lifetime structures after each processing step until after the passivation process. This $J_{0e}{}^{\text{tot.}}$ accumulates the J_0 component of the locally laser-doped regions $J_0{}^{\text{LD}}$ and the ideally intact area in between the laser-doped lines $J_{0e}{}^{\text{Control}}$. The change in the emitter recombination current density of the control samples after a sequence of processes is presented with hollow symbols, as shown in Fig. 5. The initial single-side J_{0e} of the samples in the as-fired state was on average 80–90 fA/cm^2. Upon laser doping, the total J_{0e} of the laser-doped surface increased, peaking at the laser speed of 3 m/s (sheet resistance ∼37 Ω/□) at about 190 fA/cm^2, then decreasing to about 165 fA/cm^2 for the laser profiles with ∼69 Ω/□ (6 m/s). This trend could be explained considering the interplay among the three main pathways for minority carrier loss at the laser-doped side of the samples: Auger recombination, surface recombination in the exposed laser-doped region, and nonradiative (SRH) recombination through LasIDs in the small bulk volume of the laser-doped region and at the edges. At lower laser speeds, while a high surface dopant density and a deeper profile induce greater Auger recombination rates, such dopant profiles favor minority carrier shielding from recombination at the exposed silicon surface with high SRVs. The latter is likely the dominant recombination pathway of all and, therefore, as the laser speed increases up to 3 m/s, for which surface dopant density is reduced and profiles get shallower, the surface recombination causes increased emitter recombination current density $J_0{}^{\text{tot.}}$. It is also possible that at higher laser speeds, due to rapid cooling of the melted silicon region, more defects are generated, contributing to carrier loss through SRH recombination. As the laser speed is further increased, further decrease in the surface dopant density and profile depth induces lower Auger recombination rate as well as the reduced total number of defects formed in the laser-doped region due to its reduced volume fraction, causes a drop in $J_{0e}{}^{\text{tot.}}$, whereas the surface recombination rate is still high.

It is noteworthy that these $J_{0e}{}^{\text{tot.}}$ values, after the laser-doping step, for the laser speeds 2–6 m/s are expected to reduce by

56–72 fA/cm^2, in the case where a more industrially relevant 1.3 mm spacing between laser lines is considered as opposed to 500 μm used in this study.

The ${J_0}_e^{\text{Control}}$ of the control samples remained almost unchanged after laser doping. While it was somewhat reduced after implementing AHP and 680 °C firing methods, it slightly increased in the case of 400 °C annealing passivation treatment, indicating that the 400 °C annealing process leads to a slight reduction in the effectiveness of surface passivation.

The largest reduction in the ${J_0}_e^{\text{tot.}}$ is achieved for AHP for almost all the laser-doping conditions [see Fig. 5(a)], decreasing it to values about 27–60 fA/cm^2 higher than the initial as-fired state, whereas 400 °C annealing shows the smallest improvement, except for the heavier and deeper laser-doped profiles (i.e., 0.5 and 1 m/s laser speeds) for which 680 °C firing was less effective, a similar behavior as for the ΔN_{leq} trend (see Fig. 4).

When considering the change in ${J_0}_e^{\text{tot.}}$, the change in its supposedly intact control region ${J_0}_e^{\text{Control}}$ needs to be taken into account when assessing the passivation process's effectiveness on J_0^{LD}. The overall decrease in ${J_0}_e^{\text{tot.}}$ can be partially due to a reduction in ${J_0}_e^{\text{Control}}$ in the AHP and 680 °C firing cases. To examine this, the changes in J_0^{LD} were estimated using [48]

$$ {J_0}_e^{\text{tot.}} = f^{\text{LD}} \times J_0^{\text{LD}} + \left(1 - f^{\text{LD}}\right) \times {J_0}_e^{\text{Control}} \quad (3) $$

where f^{LD} is the area fraction of the laser-doped region on the surface of the laser-doped samples.

Using (3), the J_0^{LD} is estimated, representing the recombination current density in the laser-doped region. We note that J_0^{LD} values calculated here include the total J_0 contributions from the edge areas in the laser-doped region, this influence has been shown to be significant [19], as well as the central fully melted region with a nonnegligible nonradiative recombination contribution. It should be further noted that due to the proximity of the laser lines created on the lifetime test structures, with a spacing of 500 μm, it is likely that further damage is also made on the surrounding areas in between the laser-doped lines, not visible using an optical microscope. This potential invisible damage can increase the J_0 of this supposedly intact region to a value different from what is used in the above equation, ${J_0}_e^{\text{Control}}$, extracted from the non laser-doped control samples of the silicon wafers. The extent of this discrepancy can be dependent on the applied LasID passivation treatment. Taking this effect into account, it is likely that the presented values of J_0^{LD}, as shown in Fig. 5(b), are overestimated. Therefore, the extracted values through (3) are for comparative study of different LasIDs passivation methods and do not necessarily provide accurate values for J_0^{LD}.

The increasing trend in the calculated J_0^{LD} with laser speed up to 3 m/s follows those predicted by the modeling at very high SRV representing that of the unpassivated and metal–silicon interface [see Fig. 2(c)]. This is conceivable noting the decrease in the surface dopant density and dopant profile depth as the laser speed increases [see Fig. 2(a)]. After passivation treatment is performed, a similar trend in the J_0^{LD} value with increasing laser speed is observed as that before passivation for almost all the three approaches. However, the actual value of J_0^{LD} is reduced to a different extent for the different passivation treatments. A similar trend may be due to yet the high SRVs in the laser-doped region still being the dominant recombination pathway (since the silicon surface in the laser-doped region is still exposed); however, the decrease in the J_0^{LD} value for almost all laser conditions could be potentially due to different extent of LasID annihilation in the small bulk volume of the laser-doped region or at the edges. The latter effect is likely greater at higher laser speeds as a larger number of such defects may have formed. The causes for the larger recombination current densities calculated for the laser-doped regions J_0^{LD} in Fig. 5(c), in particular after the passivation state, as compared with the simulation results in Fig. 2(c), where the latter includes contributions from the increased Auger and surface recombination, can be multiple. It can be due to underestimation of the region damaged by the laser processing beyond what is visible by the optical microscope, incomplete passivation of laser-induced bulk defects within the fully molten zone lumped into the J_0^{LD} of the emitter having a different dopant type as the base as well as the ineffectiveness of any of the investigated post-treatment methods in the annihilation of the detrimental edge damages with high possibilities of the absence of minority carrier shielding effect at around the edge damages.

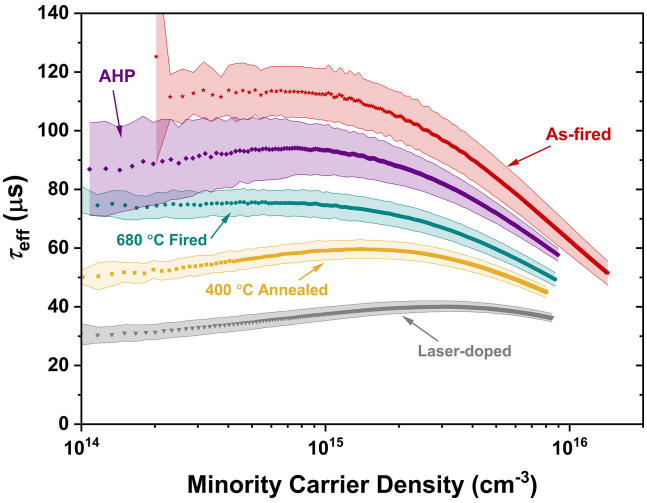

Fig. 6. Example of effective lifetime curves versus minority carrier density in the as-fired, laser-doped, and after LID test states for samples laser doped with laser head scan speed of 4 m/s. Uncertainties are calculated, as described in Fig. 3(b).

D. LasID Passivation Techniques Impact on LID

We then assessed the extent to which these different LasID passivation techniques can also alleviate LID in both control and laser-doped samples. The extent of deterioration in the effective lifetimes of the same samples, which went through laser doping and then passivation post treatments, was investigated by implementing an accelerated degradation test, representing LID [33]. The summary of changes in the effective lifetimes for the samples laser doped at 4 m/s is included in Fig. 6.

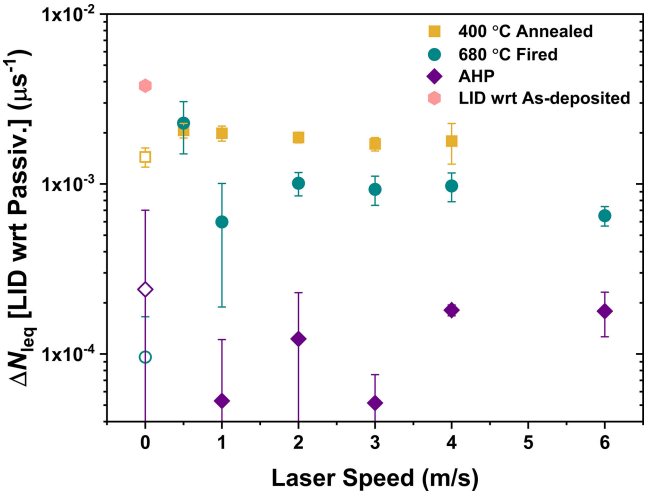

Fig. 7. ΔN_{leq} values for the control and laser-doped samples calculated for the LID state with respect to the passivated state.

It can be clearly seen that AHP more effectively mitigates LID in the laser-doped samples as compared with the other two approaches. At this laser condition of 4 m/s, for instance, the average effective lifetime (at 9.4×10^{14} cm^{-3}) for AHP passivated samples dropped on average by $\sim$18.9 μs with respect to the initial as-fired state, whereas those of 680 °C fired and 400 °C annealed samples by $\sim$37.5 μs and $\sim$53.3 μs, respectively. Overall, the AHP treatment suppressed the effective lifetime degradation in the laser-doped samples to a maximum of only 3.8% (with respect to the passivated state), as opposed to 13.7% and 15.9% for the firing and BFA treatments, respectively. For the control samples, the average effective lifetime (at 9.4×10^{14} cm^{-3}) of the ones treated by AHP decreased after the degradation test by only $\sim$1.4% as opposed to $\sim$4.2% and $\sim$15.8% for 680 °C firing and 400 °C annealing treatments, respectively.

To better understand these observations, the ΔN_{leq} values calculated after the degradation test with respect to the passivated state are presented in Fig. 7. For the laser-doped samples treated by AHP, total ΔN_{leq}, including the changes in the control sample, remained lower than that of the 680 °C fired samples by at least a factor of 2. It is noteworthy that the ΔN_{leq} of the control samples, as well as the laser-doped samples, treated by AHP is an order of magnitude lower than that of the p-type Cz control samples that went straight through the degradation test without an initial firing step (indicated with a hexagonal data point in Fig. 7). The initial effective lifetime of the latter nonfired sample was 128$\pm$7.2 μs. It is important to mention that even though the τ_{eff} of this sample is relatively high in the order of the fired ones, the surface effect is removed for its ΔN_{leq} calculation. The largest total ΔN_{leq} values after the degradation test were observed for the 400 °C annealed samples. This is strong evidence of the overall formation of fewer active defects (both in bulk and at the surface) after the degradation test in the AHP-treated samples, both in the control and laser-doped samples. Note that the ΔN_{leq} changes after LID in the laser-doped samples also include the change in the effective defect density of the background defects other than LasIDs. A large number of defects were formed in the control regions (i.e., non laser-doped) of the 400 °C furnace annealed samples compared with the control samples that went through other passivation processes. The increase in ΔN_{leq} of the laser-doped regions in the furnace firing case can potentially be due to unstable passivation of LasIDs by 680 °C firing, which may become activated under illumination during the degradation test or inability of the firing step in effective deactivation of the LID precursor defect(s) present in the laser-doping affected regions, or a combination of the two. Considering the high-temperature (i.e., 150 °C) illumination process conducted for rapid degradation investigation of the samples, another speculation could be that, during laser doping, further hydrogen is released locally into silicon from the dielectric, a subsequent furnace firing distributes this hydrogen and, as a result, activates an LeTID mechanism, reported to be also present in p-type Cz silicon [49]. The migration of charged hydrogen species and their subsequent interaction with dopant atoms in the silicon bulk and diffusion layer has been proposed to play a role in LeTID [50].

It is noteworthy that the slow 400 °C furnace annealing post treatment has been previously applied—using commercial furnaces, such as Centrotherm—on laser-doped samples for LasID annihilation purposes [23]. Here, we present results indicating not only that this slow furnace annealing approach is not necessarily the most effective approach in passivating LasIDs but also activates recombination active defects and/or increases their precursor concentration in the bulk, which in turn possibly caused the greater extent of overall degradation in the p-type Cz grown silicon.

The changes in the estimated $J_0{}^{\mathrm{LD}}$ after the LID test were then assessed. After LID, the 400 °C annealing post treatment resulted in a minimal drop in the recombination current density of the laser-doped regions for all the laser conditions. AHP resulted in an increase in the $J_0{}^{\mathrm{LD}}$ (these data are not shown since their difference with respect to the data provided in Fig. 5(a) is not remarkable). Comparing the hollow data points in Figs. 5(a) and 8, while 680 °C firing process did not affect the control sample emitter recombination current density $J_0{}^{\mathrm{tot.}}$, 400 °C annealing and AHP caused a degradation and improvement, respectively. It is important that, even though 400 °C annealing prevented noticeable rise in $J_0{}^{\mathrm{LD}}$ after LID, the effective $J_0{}^{\mathrm{LD}}$ recovery upon implementing AHP after laser doping and prior to the LID step led to overall outperformance of AHP with overall lower $J_0{}^{\mathrm{LD}}$ values for the samples. In this regard, 680 °C firing stood second. The results associated with the total $J_0{}^{\mathrm{tot.}}$ after degradation test are given in Fig. 8.

It is noteworthy that the layer combination of the dielectric stack and its thickness has been shown to be critical in determining the extent to which LasIDs are formed, impacting the device performance [21], [51]. It has been demonstrated, for a range of laser conditions, that degradation in the minority carrier lifetime and, thus, the implied V_{OC} of the laser-doped samples is reduced when a thin layer of silicon oxide (SiO_2) is deposited underneath the antireflection coating SiN_x [21], [51]. We speculate that deposition of a thin layer of SiO_2, with an optimized thickness, under the SiN_x layer can potentially reduce

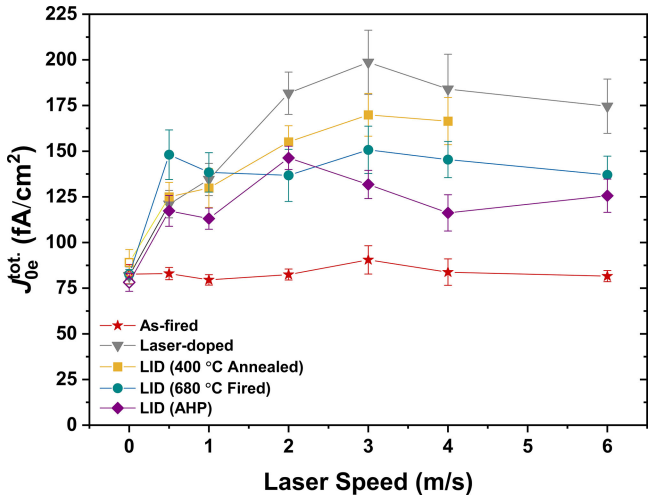

Fig. 8. Total J_{0e} (combined emitter recombination current density of the laser-doped regions and the regions in between the laser lines) of the laser-doped side of the lifetime structures for the final state of the processes, after degradation test, gone through different passivation treatments. The hollow data points represent the average of single-side J_{0e} of the control regions for all the laser-doping speeds and all the passivation approaches (18 data points) for the as-fired and laser-doped states. The error bars are calculated in the same way as those in Fig. 5(a).

the damage induced by the laser-doping processing conditions used here, particularly that caused by the notorious edge effects.

A potential implication of implementing low-temperature AHP as an effective LasID passivation technique in LDSE technology is to deploy it as a sintering process for the plated metal grid, enhancing both V_{OC} and reducing contact resistance. This way a single AHP step can simultaneously efficiently passivate the defects created in the laser-doping step, sinter the metallized fingers, and prevent LID.

At last, it is noteworthy to mention that preliminary results, not presented here, show that in the absence of SiO_2, as in this work, when no prefiring step is performed, a single firing process after the laser-doping step is more effective than the other two treatment approaches, AHP and BFA, which is expected. However, a subsequent AHP after the single firing step after the laser-doping process can potentially further improve the minority carrier's effective lifetime recovery and eliminate LID.

IV. Conclusion

We investigated the effectiveness of various post laser-doping treatments in passivating LasIDs. For almost all the laser-doping conditions investigated in this study, annealing under high illumination intensities (AHP) was shown to be effective in mitigating laser-induced damage, resulting in a small remaining lifetime-equivalent defect density (ΔN_{leq}). Depending on the laser condition, it led to ΔN_{leq} values for AHP 45%–84% lower than those of furnace firing treatment and 65%–92% lower than those of BFA approach (extracted after the passivation step with respect to the initial fired state). AHP reduced the total J_0 of the laser-doped surface by up to 40%, in comparison to the maximum of 32% and 17% for firing and BFA, respectively, depending on the laser-doping condition.

Upon LID testing, the AHP treatment was shown to suppress the effective lifetime degradation in the laser-doped samples to a maximum of only 3.8% (with respect to the passivated state), as opposed to 13.7% and 15.9% for the firing and BFA treatments, respectively. A large effective lifetime degradation of 15.8% was observed in the non laser-doped control samples that went through BFA, similar in magnitude to the degradation in the corresponding laser-doped samples treated through BFA. This was significantly higher than for the control samples treated with the firing furnace and AHP process, where degradation was only ~4.2% and ~1.4%, respectively. This indicates that the 400 °C belt furnace treatment increases the susceptibility of the bulk (non laser-doped regions) to LID in comparison with the other two passivation methods.

Overall, AHP provided improved passivation over more common passivation treatments, furnace firing, and annealing, resulting in the largest J_0 recovery and lowest ΔN_{leq} upon laser doping and subsequently led to the lowest extent of LID. AHP is also a more desirable passivation method considering the thermal budget of the LasID passivating technique.

Acknowledgment

The authors would like to thank Associate Prof. Z. Hameiri and Dr. M. Kim for fruitful discussion, Dr. M. Wright for reviewing of the manuscript, and the Solar Industry Research Facility Team at the University of New South Wales for contribution to sample fabrication. The Australian Government does not accept responsibility for any information or advice contained herein.

References

[1] J. Zhao, A. Wang, and M. A. Green, "24·5% efficiency silicon PERT cells on MCZ substrates and 24·7% efficiency PERL cells on FZ substrates," *Prog. Photovolt.*, vol. 7, no. 6, pp. 471–474, 1999, doi: 10.1002/(sici)1099-159x(199911/12)7:6<471::aid-pip298>3.0.co;2-7.

[2] X. Yang, J. Bullock, Q. Bi, and K. Weber, "High efficiency n-type silicon solar cells featuring passivated contact to laser doped regions," *Appl. Phys. Lett.*, vol. 106, no. 11, 2015, Art. no. 113901, doi: 10.1063/1.4915326.

[3] U. Angel *et al.*, "Progress on large area n-type silicon solar cells with front laser doping and a rear emitter," *Prog. Photovolt.*, vol. 24, no. 8, pp. 1149–1156, 2016, doi: 10.1002/pip.2767.

[4] B. S. Tjahjono *et al.*, "High efficiency solar cell structures through the use of laser doping," in *Proc. 22nd Eur. Photovolt. Sol. Energy Conf.*, 2007, pp. 966–969.

[5] B. Hallam *et al.*, "Efficiency enhancement of i-PERC solar cells by implementation of a laser doped selective emitter," *Sol. Energy Mater. Sol. Cells*, vol. 134, pp. 89–98, 2015. [Online]. Available: https://doi.org/10.1016/j.solmat.2014.11.028

[6] S. Hopman *et al.*, "Study on laser parameters for silicon solar cells with LCP selective emitters," in *Proc. 24th Eur. Photovolt. Sol. Energy Conf.*, 2009, pp. 1072–1076.

[7] S. W. Glunz *et al.*, "The irresistible charm of a simple current flow pattern—25% with a solar cell featuring a full-area back contact," in *Proc. 31st Eur. Photovolt. Sol. Energy Conf. Exhib.*, 2015, pp. 259–263, doi: 10.4229/EUPVSEC20152015-2BP.1.1.

[8] A. Rohatgi *et al.*, "Fabrication and modeling of high-efficiency front junction N-type silicon solar cells with tunnel oxide passivating back contact," *IEEE J. Photovolt.*, vol. 7, no. 5, pp. 1236–1243, Sep. 2017.

[9] International Technology Roadmap for Photovoltaic, 2021. [Online]. Available: https://itrpv.vdma.org/en/

[10] T. Röder *et al.*, "0.4% absolute efficiency gain of industrial solar cells by laser doped selective emitter," in *Proc. 34th IEEE Photovolt. Specialists Conf.*, 2009, pp. 871–873, doi: 10.1109/PVSC.2009.5411149.

[11] R. Chen *et al.*, "23.83% efficient mono-PERC incorporating advanced hydrogenation," *Prog. Photovolt.*, vol. 28, pp. 1239–1247, Dec. 2020, doi: 10.1002/pip.3243.

[12] R. S. Davidsen *et al.*, "Black silicon laser-doped selective emitter solar cell with 18.1% efficiency," *Sol. Energy Mater. Sol. Cells*, vol. 144, pp. 740–747, 2016. [Online]. Available: https://doi.org/10.1016/j.solmat.2015.10.018

[13] Z. Wang *et al.*, "Advanced PERC and PERL production cells with 20.3% record efficiency for standard commercial p-type silicon wafers," *Prog. Photovolt.*, vol. 20, no. 3, pp. 260–268, May 2012, doi: 10.1002/pip.2178.

[14] S. R. Wenham, M. B. Edwards, A. J. Lennon, P. C. Hsiao, and B. S. Tjahjono, "Solar cell metallisation and interconnection method," WIPO Patent WO 2014/117216 A1, Nov. 2016.

[15] P. M. Mooney, R. T. Young, J. Karins, Y. H. Lee, and J. W. Corbett, "Defects in laser damaged silicon observed by DLTS," *Phys. Status Solidi*, vol. 48, no. 1, pp. K31–K34, 1978, doi: 10.1002/pssa.2210480144.

[16] D. Kray *et al.*, "Laser-doped silicon solar cells by laser chemical processing (LCP) exceeding 20% efficiency," in *Proc. 33rd IEEE Photovolt. Specialists Conf.*, 2008, pp. 1–3, doi: 10.1109/PVSC.2008.4922848.

[17] M. Ametowobla, G. Bilger, J. R. Köhler, and J. H. Werner, "Laser induced lifetime degradation in p-type crystalline silicon," *J. Appl. Phys.*, vol. 111, no. 11, 2012, Art. no. 114515, doi: 10.1063/1.4725191.

[18] H. T. Nguyen *et al.*, "Dislocations in laser-doped silicon detected by microphotoluminescence spectroscopy," *Appl. Phys. Lett.*, vol. 107, no. 2, 2015, Art. no. 022101, doi: 10.1063/1.4926360.

[19] M. Ernst, J. D. Huyeng, D. Walter, K. C. Fong, and A. Blakers, "Unravelling the origins of contact recombination for localized laser-doped contacts," in *Proc. 7th World Conf. Photovolt. Energy Convers.*, 2018, pp. 2195–2199, doi: 10.1109/PVSC.2018.8547383.

[20] A. Sugianto, B. S. Tjahjono, J. H. Guo, and S. R. Wenham, "Impact of laser induced defects on the performance of solar cells using localised laser doped regions beneath the metal contacts," in *Proc. 22nd Eur. Photovolt. Sol. Energy Conf. Exhib.,* 2007, pp. 1759–1762.

[21] L. Xu *et al.*, "The impact of SiO_2/SiN_x stack thickness on laser doping of silicon solar cell," *IEEE J. Photovolt.*, vol. 4, no. 2, pp. 594–600, Mar. 2014.

[22] S. Wang *et al.*, "Advanced passivation of laser-doped and grooved solar cells," *Sol. Energy Mater. Sol. Cells*, vol. 193, pp. 403–410, 2019. [Online]. Available: https://doi.org/10.1016/j.solmat.2019.01.025

[23] B. Hallam *et al.*, "Hydrogen passivation of laser-induced defects for laser-doped silicon solar cells," *IEEE J. Photovolt.*, vol. 4, no. 6, pp. 1413–1420, Nov. 2014.

[24] Z. Sun and M. C. Gupta, "Laser induced defects in silicon solar cells and laser annealing," in *Proc. IEEE 43rd Photovolt. Specialists Conf.*, 2016, pp. 713–716, doi: 10.1109/PVSC.2016.7749694.

[25] Z. Sun and M. C. Gupta, "A study of laser-induced surface defects in silicon and impact on electrical properties," *J. Appl. Phys.*, vol. 124, no. 22, 2018, Art. no. 223103, doi: 10.1063/1.5058143.

[26] J. Lindroos and H. Savin, "Review of light-induced degradation in crystalline silicon solar cells," *Sol. Energy Mater. Sol. Cells*, vol. 147, pp. 115–126, 2016. [Online]. Available: https://doi.org/10.1016/j.solmat.2015.11.047

[27] J. Schmidt, K. Bothe, V. V. Voronkov, and R. Falster, "Fast and slow stages of lifetime degradation by boron–oxygen centers in crystalline silicon," *Phys. Status Solidi*, vol. 257, no. 1, Jan. 2020, Art. no. 1900167, doi: 10.1002/pssb.201900167.

[28] B. Hallam *et al.*, "Eliminating light-induced degradation in commercial p-type czochralski silicon solar cells," *Appl. Sci.*, vol. 8, no. 1, 2018, Art. no. 10, doi: 10.3390/app8010010.

[29] J. Schmidt and K. Bothe, "Structure and transformation of the metastable boron- and oxygen-related defect center in crystalline silicon," *Phys. Rev. B*, vol. 69, no. 2, pp. 241071–241078, Jan. 2004, doi: 10.1103/PhysRevB.69.024107.

[30] A. Herguth, G. Schubert, M. Kaes, and G. Hahn, "A new approach to prevent the negative impact of the metastable defect in boron doped CZ silicon solar cells," in *Proc. IEEE 4th World Conf. Photovolt. Energy Conf.*, 2006, pp. 940–943, doi: 10.1109/WCPEC.2006.279611.

[31] N. Nampalli, B. J. Hallam, C. E. Chan, M. D. Abbott, and S. R. Wenham, "Influence of hydrogen on the mechanism of permanent passivation of boron–oxygen defects in p-type czochralski silicon," *IEEE J. Photovolt.*, vol. 5, no. 6, pp. 1580–1585, Nov. 2015.

[32] B. J. Hallam *et al.*, "Advanced hydrogenation of dislocation clusters and boron-oxygen defects in silicon solar cells," *Energy Procedia*, vol. 77, pp. 799–809, 2015. [Online]. Available: https://doi.org/10.1016/j.egypro.2015.07.113

[33] P. Hamer, B. Hallam, M. Abbott, and S. Wenham, "Accelerated formation of the boron–oxygen complex in p-type Czochralski silicon," *Phys. Status Solidi—Rapid Res. Lett.*, vol. 9, no. 5, pp. 297–300, May 2015, doi: 10.1002/pssr.201510064.

[34] B. J. Hallam *et al.*, "Development of advanced hydrogenation processes for silicon solar cells via an improved understanding of the behaviour of hydrogen in silicon," *Prog. Photovolt.*, vol. 28, pp. 1217–1238, 2020, doi: 10.1002/pip.3240.

[35] B. J. Hallam *et al.*, "Advanced bulk defect passivation for silicon solar cells," *IEEE J. Photovolt.*, vol. 4, no. 1, pp. 88–95, Jan. 2014.

[36] D. C. Walter *et al.*, "Effect of rapid thermal annealing on recombination centres in boron-doped Czochralski-grown silicon," *Appl. Phys. Lett.*, vol. 104, no. 4, Jan. 2014, Art. no. 042111, doi: 10.1063/1.4863674.

[37] N. Nampalli *et al.*, "Multiple pathways for permanent deactivation of boron-oxygen defects in p-type silicon," *Sol. Energy Mater. Sol. Cells*, vol. 173, pp. 12–17, 2017. [Online]. Available: https://doi.org/10.1016/j.solmat.2017.06.041

[38] Z. Hameiri *et al.*, "Low-absorbing and thermally stable industrial silicon nitride films with very low surface recombination," *IEEE J. Photovolt.*, vol. 7, no. 4, pp. 996–1003, Jul. 2017.

[39] D. Bredemeier, D. C. Walter, R. Heller, and J. Schmidt, "Impact of hydrogen-rich silicon nitride material properties on light-induced lifetime degradation in multicrystalline silicon," *Phys. Status Solidi—Rapid Res. Lett.*, vol. 13, no. 8, Aug. 2019, Art. no. 1900201, doi: 10.1002/pssr.201900201.

[40] S. Wilking *et al.*, "High speed regeneration of BO-defects: Improving long-term solar cell performance within seconds," in *Proc. 29th Eur. Photovolt. Sol. Energy Conf. Exhib.*, 2014, pp. 366–372, doi: 10.4229/EUPVSEC20142014-2BP.1.2.

[41] H. F. W. Dekkers, S. De Wolf, G. Agostinelli, F. Duerinckx, and G. Beaucarne, "Requirements of PECVD SiNx:H layers for bulk passivation of mc-Si," *Sol. Energy Mater. Sol. Cells*, vol. 90, no. 18/19, pp. 3244–3250, 2006. [Online]. Available: https://doi.org/10.1016/j.solmat.2006.06.024

[42] K. R. McIntosh *et al.*, "An examination of three common assumptions used to simulate recombination in heavily doped silicon," in *Proc. 28th Eur. Photovolt. Sol. Energy Conf. Exhib.*, 2013, pp. 1672–1679.

[43] EDNA 2, PV Lighthouse. [Online]. Available: https://www2.pvlighthouse.com.au/calculators/EDNA%202/EDNA%202.aspx

[44] D. N. R. Payne *et al.*, "Acceleration and mitigation of carrier-induced degradation in p-type multi-crystalline silicon," *Phys. Status Solidi—Rapid Res. Lett.*, vol. 10, no. 3, pp. 237–241, Mar. 2016. [Online]. Available: https://doi.org/10.1002/pssr.201510437

[45] R. A. Sinton and A. Cuevas, "A quasi-steady-state open-circuit voltage method for solar cell characterization," in *Proc. 16th Eur. Photovolt. Sol. Energy, Conf.*, 2000, pp. 1152–1155.

[46] A. Richter, F. Werner, A. Cuevas, J. Schmidt, and S. W. Glunz, "Improved parameterization of auger recombination in silicon," *Energy Procedia*, vol. 27, pp. 88–94, 2012. [Online]. Available: https://doi.org/10.1016/j.egypro.2012.07.034

[47] A. Herguth, "On the lifetime-equivalent defect density: Properties, application, and pitfalls," *IEEE J. Photovolt.*, vol. 9, no. 5, pp. 1182–1194, Sep. 2019.

[48] C. Dang *et al.*, "Investigation of laser ablation induced defects in crystalline silicon solar cells," *Energy Procedia*, vol. 55, pp. 649–655, 2014. [Online]. Available: https://doi.org/10.1016/j.egypro.2014.08.040

[49] F. Fertig *et al.*, "Mass production of p-type cz silicon solar cells approaching average stable conversion efficiencies of 22%," *Energy Procedia*, vol. 124, pp. 338–345, 2017. [Online]. Available: https://doi.org/10.1016/j.egypro.2017.09.308

[50] D. Chen *et al.*, "Hydrogen-induced degradation: Explaining the mechanism behind light- and elevated temperature-induced degradation in n- and p-type silicon," *Sol. Energy Mater. Sol. Cells*, vol. 207, 2020, Art. no. 110353. [Online]. Available: https://doi.org/10.1016/j.solmat.2019.110353

[51] Z. Hameiri, T. Puzzer, L. Mai, A. B. Sproul, and S. R. Wenham, "Laser induced defects in laser doped solar cells," *Prog. Photovolt.*, vol. 19, no. 4, pp. 391–405, 2011, doi: 10.1002/pip.1043.